The interplay of symmetry and scattering phase in second harmonic generation from gold nanoantennas

Gennaro, Sylvain D; Rahmani, Mohsen; Vincenzo, Giannini; Aouani, Heykel; Sidiropoulos, Themistoklis P H; Navarro-Cia, Miguel; Maier, Stefan A.; Oulton, Rupert F.

DOI:
10.1021/acs.nanolett.6b02485

Document Version
Peer reviewed version

Citation for published version (Harvard):
Gennaro, SD, Rahmani, M, Vincenzo, G, Aouani, H, Sidiropoulos, TPH, Navarro-Cia, M, Maier, SA & Oulton, RF 2016, 'The interplay of symmetry and scattering phase in second harmonic generation from gold nanoantennas', *Nano Letters*, vol. 16, no. 8, pp. 5278-5285. https://doi.org/10.1021/acs.nanolett.6b02485

The interplay of symmetry and scattering phase in second harmonic generation from gold nano-antennas

Sylvain D. Gennaro[1]*, Mohsen Rahmani[1]*, Vincenzo Giannini[1], Heykel Aouani[1], Themistoklis P. H. Sidiropoulos[1], Miguel Navarro-Cía[2], Stefan A. Maier[1], Rupert F. Oulton[1]†

1. The Blackett Laboratory, Department of Physics, Imperial College London, London SW7 2AZ, UK

2. School of Physics and Astronomy, University of Birmingham, Birmingham B15 2TT, UK

Supplementary Information

Nonlinear phenomena are central to modern photonics but, being inherently weak, typically require gradually accumulation over several millimetres. For example, second harmonic generation (SHG) is typically achieved in thick transparent nonlinear crystals by phase-matching energy exchange between light at initial, ω, and final, 2ω, frequencies. Recently, metamaterials imbued with artificial nonlinearity from their constituent nano-antennas have generated excitement by opening the possibility of wavelength-scale nonlinear optics. However, the selection rules of SHG typically prevent dipole emission from simple nano-antennas, which has led to much discussion concerning the best geometries; for example those breaking centro-symmetry or incorporating resonances at multiple harmonics. In this work we explore the use of both nano-antenna symmetry and multiple harmonics to control the strength, polarisation and radiation pattern of SHG from a variety of antenna configurations incorporating simple resonant elements tuned to light at both ω and 2ω. We use a microscopic description of the scattering strength and phases of these constituent particles, determined by their relative positions, to accurately predict the SHG radiation observed in our experiments. We find that the 2ω particles radiate dipolar SHG by near-field coupling to the ω particle, which radiates SHG as a quadrupole. Consequently, strong linearly polarised dipolar SHG is only possible for non-centro-symmetric antennas that also minimize interference between their dipolar and quadrupolar responses. Metamaterials with such intra-antenna phase and polarisation control could enable compact nonlinear photonic nanotechnologies.

A recurring theme in optics and photonics is the ability of metal nanostructures to imbue artificial materials with new functions. Metallic nano-antennas[1], so-called meta-atoms, are the building blocks of such metamaterials that boast unusual linear[2,3] and nonlinear[4–6] characteristics. Recently, nonlinear metamaterials have generated considerable excitement; while nonlinear effects in natural materials must gradually accumulate weak nonlinearity across macroscopic crystal dimensions, a small volume of metamaterial[7,8], and even isolated nano-antennas[9–12], can create a surprisingly strong effect. This capability stems from additional nanoscopic degrees of freedom that include couplings between the constituent nanoparticles within nano-antennas or between nano-antennas and material resonances[7–9,13,14]. Moreover, metamaterials do not necessarily follow the convention that the strength of nonlinearity in certain materials stems from their linear properties[15,16]. This suggests a departure from conventional physical limitations in nonlinear optics. Metamaterials with tailored nonlinear responses look set to provide exceptional flexibility in applications such as super-resolution

imaging[17], efficient frequency conversion[18], optical switching and coherent optical control at the nanoscale[19,20].

Second harmonic generation (SHG) from metal nano-antennas is a particularly interesting effect as metals belong to a class of materials with symmetry-forbidden even order nonlinearity. Although it has been known for some time that the broken symmetry of a metal's surface produces a second order nonlinear response, resonant metal nanoparticles can significantly enhance SHG using a number of additional techniques, for example: exploiting enhanced absorption at Fano resonances[21–23]; breaking the symmetry with the nano-antenna's own geometry[24,25]; in-plane external phase control of nano-antenna arrays to direct and focus SHG[7,8]; and designing nano-antennas with coupled nanoparticles that are resonant at both pump and SHG frequencies[11,14,25–28].

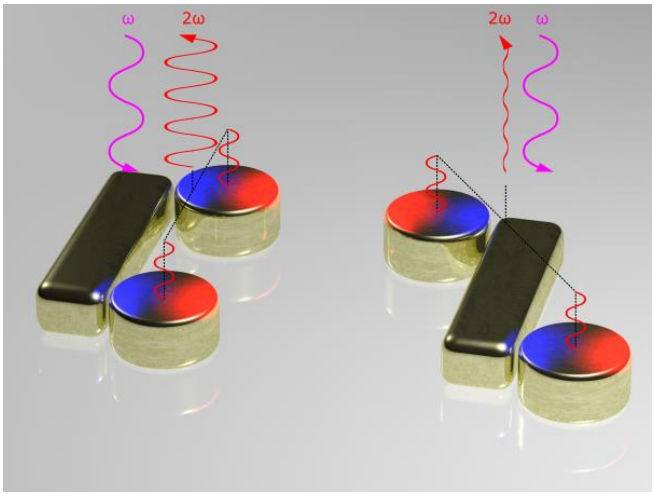

Figure 1. Illustration of SHG interference in multi-resonant gold nano-antennas. The image shows two of the nano-antenna configurations investigated (CIII and CIV). The nano-antennas are initially excited through a bar shaped particle (ω-particle). The two discs (2ω-particles) in the nano-antenna on the left radiate in phase leading to bright and directional SHG. Meanwhile, the nano-antenna on the right supresses SHG normal to the substrate surface as its 2ω-particles radiate out of phase.

In this paper we examine the importance of the nano-antenna configuration on SHG's strength, polarisation and emission pattern. Each nano-antenna in our investigation consists of a single ω-particle (bar) and a number of 2ω-particles (discs) tuned to the pump and second harmonic frequencies, respectively. Using these constituent particles in a range of configurations we show how the activation and deactivation of an antenna's dipole SHG emission can be understood in terms of the interference of the dipole and quadrupole sources of the antenna. For example, the location of each 2ω-particle relative to the ω-particle determines its radiation phase at the second harmonic frequency. When positioned in a non-centro-symmetric arrangement, multiple 2ω-particles constructively interfere to generate a linearly polarised and "bright" dipole SHG emission pattern (left nano-antenna in Fig. 1). However, a centro-symmetric configuration enforces destructive interference of the 2ω-particles to leave only a "dark" remnant of quadrupole scattering at the second harmonic frequency (right nano-antenna in Fig. 1). Moreover, we find that the interference of quadrupole and dipole radiation, even in non-centro-symmetric configurations, leads to much weaker SHG. We directly confirm these observations by measuring the emission patterns of individual nano-antennas in the back focal plane, which are distinctive for the various configurations considered. This work shows that in

each investigated nano-antenna the bar element drives the nonlinear polarisation while the disc elements provide the means to efficiently radiate SHG via the mutual coupling. In this sense, the 2ω-elements probe the phase of the bar's non-linear polarisation.

We investigate five different nanostructures (CI-CV) (See Fig. 2a). Configurations CI and CII re-examine the concept of incorporating multiple harmonic resonances to boost SHG emission as considered in previous work[14,25–28]. Configuration CIII shows not only how to improve the polarisation and dipole like emission patterns compared to CI and CII, but also highlights the importance of having the 2ω-elements radiating in phase. This is in contrast to CIV, which cancels dipole like emission since it is centro-symmetric. Despite being non-centro symmetric, configuration CV performs considerably worse than CIII since its quadrupole and dipole components are designed to be aligned so that they interfere. In order to fully explore the variations in SHG between the various nano-antennas investigated, we have simulated and measured their linear extinction spectra (Fig. 2b,c), their SHG spectral distribution (Fig. 2d,e), their polarisation and radiation patterns (Fig. 3, 4 and 5) at the second harmonic frequency. (Details of sample fabrication and the experimental set-up are presented at the end of this letter.) To observe SHG in our experiments, we illuminate a single isolated nano-antenna with a near diffraction limited spot at a wavelength of 1,500 nm and filter the reflected light to select only the second harmonic wavelength at 750 nm (See Figure S1). The choice to measure SHG from individual nano-antennas allows us to unambiguously assess the shape of the radiation pattern. We selected nano-antennas whose linear responses display a resonance very near the fundamental frequency, so that a similar amount of power is coupled to each nano-antenna. This will help to draw conclusions about the variations in SHG emission intensity (Fig. 6).

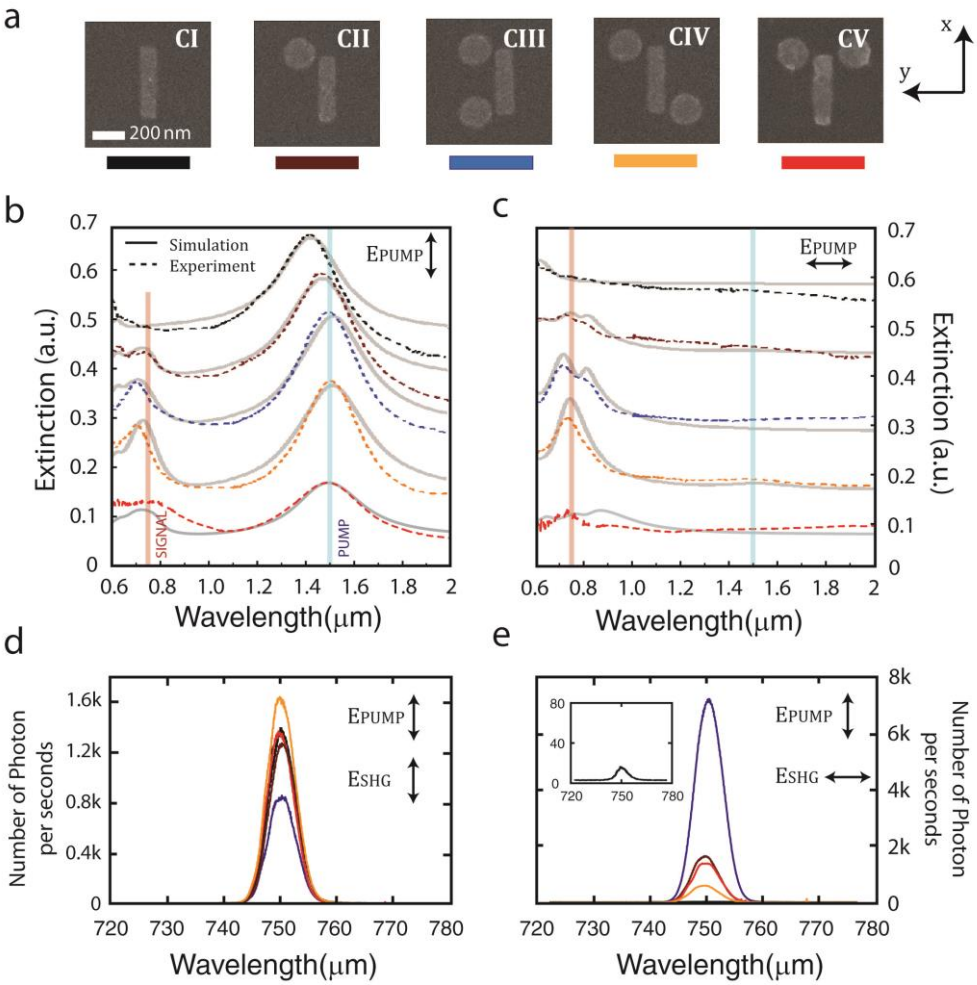

Figure 2. Linear extinction spectra and SHG of multi-resonant gold nano-antennas. a SEM images of the five nano-antenna configuration (CI-CV) considered in this work. Dimensions of the bars are 340×80×40 nm in x, y and z, respectively, while discs are the same thickness with diameters of 160 nm. The gaps between the discs and the bar are 20 nm for all cases. **b** and **c** show the measured (broken colour lines) and simulated (solid grey lines) extinction spectra for light incident parallel (x – axis) and perpendicular (y – axis) to the bar-particle, respectively. **d** and **e** show the measured SHG signals from the five configurations for a pump polarised along the bar. In d (resp. e), the SHG signal is polarised along (resp. perpendicular to) the bar. Inset of e is the SHG spectra of CI. The data have been calibrated to take into account the polarisation sensitivity of the spectrometer (See Figure S2).

Figures 2b and 2c show the linear simulated and experimental extinction spectra of the various nano-antenna configurations under consideration (Fig. 2a). The nano-antennas were designed to be doubly resonant to enhance SHG. An ω-particle is resonant near the pump wavelength of 1,500 nm and due to its bar shape only scatters the pump beam when it is polarised along the x-direction. Meanwhile the 2ω-particles, resonant near 750 nm, are discs and may scatter SHG with an arbitrary polarisation dependent upon their coupling with the bar. Indeed, Figs. 2d and 2e show that strong SHG signal emerges with a y-polarisation, perpendicular to the bar, only for the doubly resonant configurations (CII to CV in Fig. 2e). It is weakest for the bar alone (CI), as shown in the inset of Fig. 2e. The dominance of y-polarised SHG in the doubly resonant nano-

antennas reaffirm the role of the 2ω-particles in promoting SHG. In contrast, x-polarised SHG (Fig. 2d) from the nano-antennas CII, CIV and CV are comparable to the SHG of the bar alone (CI), and CIII has a supressed response. We also note that SHG decreases by over 3 orders of magnitude for a y-polarised pump (perpendicular to the bar, see Figure S3), confirming the pivotal role of the nano-antennas' resonant modes in producing SHG.

The importance of antenna symmetry is immediately apparent when comparing the larger signal from CIII with that of CIV, shown in Fig. 2e. Remarkably, even the CII nano-antenna with only a single 2ω-particle has a 2-fold improved response over CIV. It is noteworthy however, that CIV has a distinctive distribution of SHG compared to the bar alone, CI, even though they are both centro-symmetric. Moreover, despite being non-centro symmetric, CV has performance comparable to CIV. Symmetry arguments alone cannot provide insight into such observations, which is why a microscopic point of view is warranted. Indeed, we propose that the variation observed here stems from the interference of the SHG radiation from constituent particles within the antenna. The phase of the nonlinear polarisation in the bar must determine the scattering phase of 2ω-particles within a nano-antenna and thus the SHG radiation pattern and polarisation. While numerous works have considered SHG in doubly resonant nano-antennas[11,14,25–28], configurations involving multiple 2ω-particles have not been examined before, yet could be important for creating an effective nonlinear response.

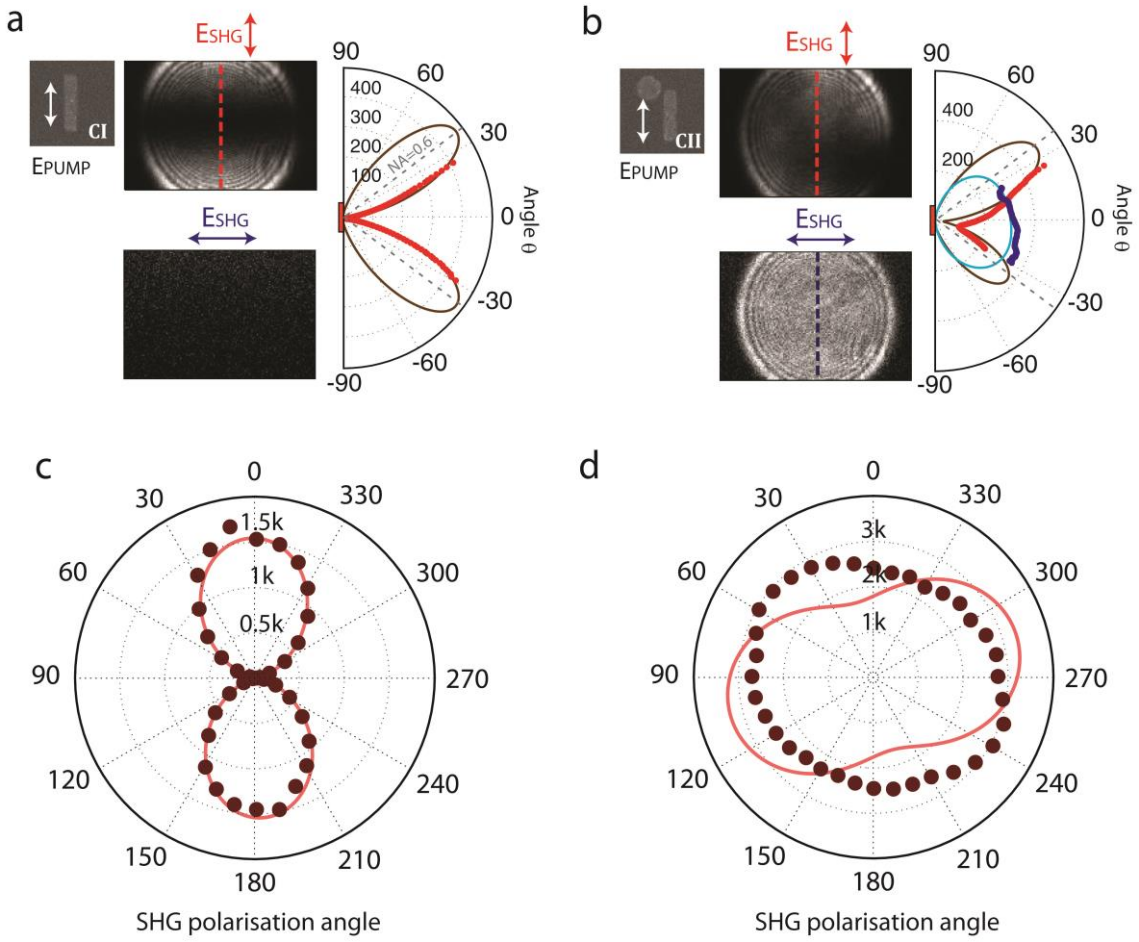

Figure 3. SHG radiation patterns and polarisations for nano-antennas CI and CII. a and **b** show the direction of SHG emission for CI and CII, respectively measured in the back focal plane of our microscope. Red (resp. blue) dots are the smoothened experimental vertical line-

scan data from the x (resp. y) - polarised back focal plane images. Brown (resp. cyan) lines are the best fit to a multi-pole model (See Note 3 and Figure S4 of Supplementary Information for model details). Units are photon counts over 75s integration time. **c** and **d** show the measured (dots) and fitted (solid line) emission polarisation for CI and CII, respectively. Units are total photons per second. The data have been calibrated to take into account the polarisation sensitivity of the spectrometer (See Figure S2).

Let us now consider in more detail the characteristics of SHG emission from the various nano-antenna configurations. Firstly, we consider the simplest CI and CII geometries, where other works on doubly resonant nano-antennas for SHG have left-off[11,14,25–28]. Figure 3a and 3b show the direction of emission in the back focal plane (BFP) of our microscope. We can see that the bar nano-antenna's (CI) SHG is from a dark quadrupole-like mode[29,30] (Fig. 3a). Since the linear polarisability of this particle is along the x-direction, negligible y-polarised SHG is recorded. For CII, which includes a single 2ω-particle, a bright dipole like response emerges (Fig. 3b) on top of the dark quadrupole response of the bar. The bright emission is of a similar strength as the dark emission as it changes completely the polarisation of SHG observed in the far field, as shown in Figs. 3c and 3d. Meanwhile, the total dark emission is about the same in both CI and CII, as shown in Fig. 2e, explaining the doubling of CII's SHG signal. Since much of the dark emission is inaccessible at normal incidence[31], the main advantage of the 2ω-particle is to increase the directionality of SHG.

We now consider geometries CIII, CIV and CV with two 2ω-particles, shown in Fig. 4. Here CIII has 2ω-particles along the long side of the bar, CIV has them arranged on opposite sides and CV has them arranged along the short side of the bar. In the case of CIII (Fig. 4a), y-polarised dipole emission constructively interferes to create brighter and more directional emission normal to the sample surface compared to CII (Fig. 3b). Meanwhile, dipole emission is completely cancelled in CIV (Fig. 4b) as both x and y polarisations have a dark response. This implies that the 2ω-particles in CIV scatter SHG out of phase leading to a 4-fold suppression of SHG compared to CIII. Differences between these nano-antennas also show up clearly in the polarisation response (Figs. 4d and 4e). While CIII is highly y-polarised from the dominant "bright" SHG from the 2ω-particles (Fig. 4d), CIV has no preferred polarisation with comparable x and y polarised "dark" emission (Fig. 4e). Since CV is non-centro symmetric (Fig. 4c and 4f), the two dipoles interfere constructively for $\boldsymbol{x}$ – polarisation, whereas they interfere destructively for $\boldsymbol{y}$ – polarisation as seen by the quadrupole emission in Fig. 4c. For $\boldsymbol{x}$ – polarisation, the dipole interferes with the quadrupole SHG from the bar, which leads to an asymmetric radiation pattern.

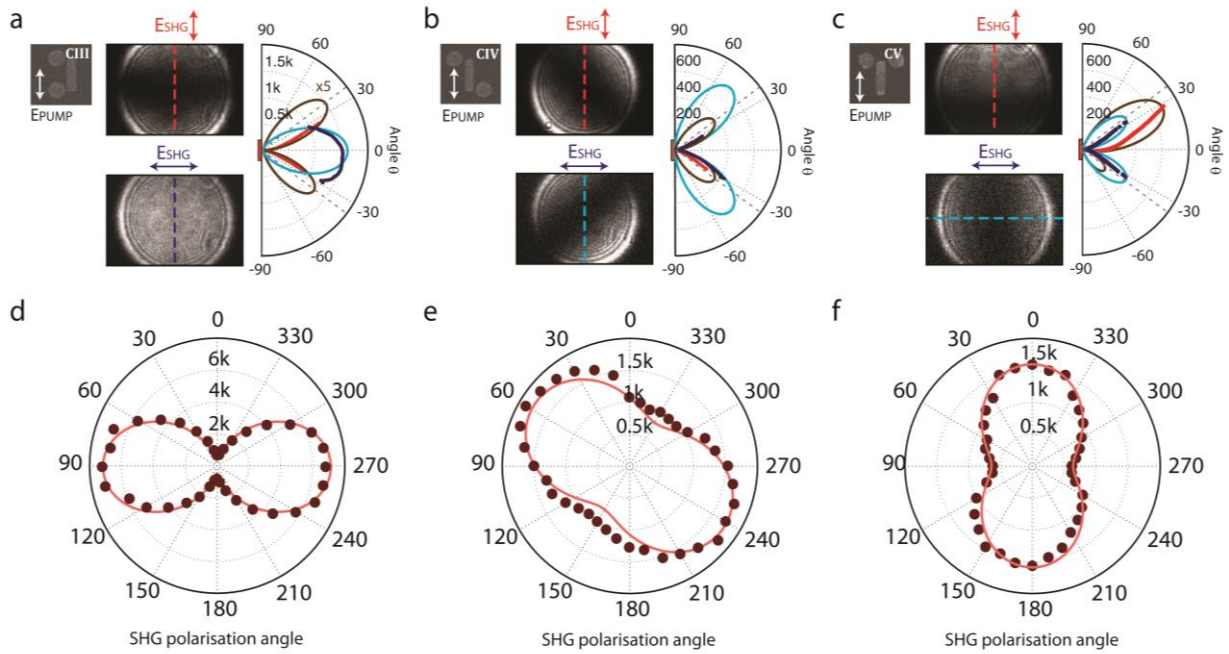

Figure 4. SHG radiation patterns and polarisations for nano-antennas CIII CIV, and CV incorporating two 2ω-particles. a, b and **c** show the direction of SHG emission for CIII, CIV and CV, respectively, measured in the back focal plane of our microscope. Red (resp. blue) dots are the smoothened experimental vertical line-scan data from the x (resp. y) - polarised back focal plane images. Brown (resp. cyan) lines are the best fit to a multi-pole model (See Note 3 and Figure S5 of Supplementary Information). Units are photon counts over 75s integration time. **d, e** and **f** show the measured (dots) and fitted (solid line) emission polarisations for CIII, CIV and CV, respectively. Units are total photons per second. The data have been calibrated to take into account the polarisation sensitivity of the spectrometer (See Figure S2).

In order to gain a deeper understanding of the microscopic view-point of CIII, CIV and CV, we have modelled the emission of SHG using a multiple dipole model to reproduce their observed back focal plane emission patterns and polarisations (See Figure S4 and Note 3). We model the structure by interfering dipoles and a quadrupole, in which the interplay of the various phases and scattering strengths reproduces the observed data. The plasmonic modes of the structure at the second harmonic frequency are described by linear coupled Lorentzian oscillators[32], such that each disc is represented by a dipole, of field amplitude, a_d, resonance frequency, ω_d, and loss rate, γ_d, which couples independently to the quadrupole mode of the bar of field amplitude, a_q, resonance frequency, ω_q, and loss rate, γ_d. The coupled system is then described by the inhomogeneous coupled equations with a source term, σ_q, such that,

$$\begin{pmatrix} \delta_d + i\gamma_d & 0 & C \\ 0 & \delta_d + i\gamma_d & C \\ C & C & \delta_q + i\gamma_q \end{pmatrix} \begin{pmatrix} a_{d1} \\ a_{d2} \\ a_q \end{pmatrix} = \begin{pmatrix} 0 \\ 0 \\ \sigma_q \end{pmatrix} \qquad (1)$$

where $\delta_d = \omega - \omega_d$ and $\delta_q = \omega - \omega_q$ are the respective detunings of dipole and quadrupole modes and C is the coupling rate between the bar and the disc modes. Here, we have assumed that the non-linear source of SHG is negligible in the discs compared to that of the bar, σ_q, since only the bar is resonant with the fundamental pump wavelength at $\lambda = 1{,}500$nm. The field amplitudes of each mode are thus given by:

$$\begin{pmatrix} a_{d1} \\ a_{d2} \\ a_q \end{pmatrix} = \frac{C\sigma_q}{C^2 - \frac{\gamma_d\gamma_q}{|\cos\psi_d||\cos\psi_q|}e^{i(\psi_d+\psi_q)}} \begin{pmatrix} 1 \\ 1 \\ i\frac{\gamma_d}{C}\frac{e^{i\psi_d}}{\cos\psi_d} \end{pmatrix} \quad (2)$$

Where the phases of dipoles and quadrupole are given by, $\tan(\psi_{d/q}) = \delta_{d/q}/\gamma_{d/q}$. We note that on resonance, the quadrupole of the bar radiates $\pi/2$ out of phase with the dipole of the disc and any additional detuning of the resonance of the disc adds an extra phase shift, ψ_d, which is one of the fitting parameters in our model. The far field intensity of the antenna at a position ***r,*** is found from the electric field contributions of one or two dipoles, $a_{di}\boldsymbol{E_{di}}(\boldsymbol{r} - \boldsymbol{s_{di}}, \phi_{di}), i \in \{1,2\}$, and a quadrupole, $a_q\boldsymbol{E_q}(\boldsymbol{r} - \boldsymbol{s_q}, \phi_q)$, at positions, $\boldsymbol{s_{di/q}}$, and orientations, $\phi_{di/q}$, in the x-y plane of the antenna,

$$|\boldsymbol{E_T}(\boldsymbol{r})|^2 = \left|a_{d1}\boldsymbol{E_{d1}}(\boldsymbol{r} - \boldsymbol{s_{d1}}, \phi_{d1}) + a_{d2}\boldsymbol{E_{d2}}(\boldsymbol{r} - \boldsymbol{s_{d2}}, \phi_{d2}) + a_q\boldsymbol{E_q}(\boldsymbol{r} - \boldsymbol{s_q}, \phi_q)\right|^2 \quad (3)$$

The field distributions, $\boldsymbol{E_{d/q}}(\boldsymbol{r})$, for each interfacial dipole are described by Engheta's formula[23,33], for a substrate refractive index, n=1.5. (See Supplementary Information file for details of the model.) Using Jones matrices, with the formula given in Eq. 3, the model is simultaneously fit to the ***x*** and ***y*** polarised back focal plane emission pattern data as well as the polarisation data. The full set of parameters (See Note 5) required include the dipole positions and orientations as well as their relative phases and amplitudes, as summarized in the table T1. We note that the quadrupole orientation $\phi_q = 0$ by definition.

	CI	CII	CIII	CIV	CV
a_q	95	105	95	105	110
a_d	N/A	47	53	44	59
ϕ_{d1}	N/A	$\frac{\pi}{2} + 0.34$	$\frac{\pi}{2} + 0.34$	$\frac{\pi}{2} + 0.34$	$\frac{\pi}{2} + 0.34$
ϕ_{d2}	N/A	N/A	$\frac{\pi}{2} - 0.34$	$\pi + \frac{\pi}{2} + 0.34$	$-\frac{\pi}{2} + 0.34$
$\frac{a_q}{a_d}$	N/A	2.23	1.79	2.39	1.86
ψ_d	N/A	0.41	0.62	0.7	0.6

Table 1: **Model fitting parameters for the five nano-antenna configurations considered in this work.** Note that ϕ_{di} were fixed to comparable values for all antennas. See Note 3 for more details.

This model re-creates accurately the observed emission patterns (back focal plane) and polarisations for CI-CV (See Fig. 3, Fig. 4 and Figure S4.) The calculated parameters in each configuration from the model show fairly uniform amplitudes of quadrupoles in the range of 95-110 and dipoles in the range of 45-60. This indicates that the SHG produce by each particle within these antennas is relatively uniform and that the relative performance of each antenna is mainly due to the interference of the various radiation sources.

The simulated multi-pole positions and orientations for CIII, that generate the correct back focal plane response as shown in Fig. 4a, are shown in Figure 5a. Along the *y*-polarisation, the

two dipoles are in phase leading to constructive interference. Moreover, for the *x*-polarisation the two dipoles are out of phase, and interfere destructively with the quadrupole to reduce the bar's quadrupolar SHG emission, which is consistent with our observations in Fig. 2d and 2e. In contrast, Fig. 5b shows the simulated multi-pole positions and orientations for the CIV nano-antenna that generate the correct back focal plane response as shown in Fig. 4b. Since both *x* and *y*-polarisations are quadrupolar in nature, the two dipoles must be out of phase. Finally, in the configuration CV, the two dipoles are out of phase for the y – polarisation; however, for the x – polarisation, the two in-phase dipoles interfere with the quadrupole of the bar, leading the tilted back focal plane response observed.

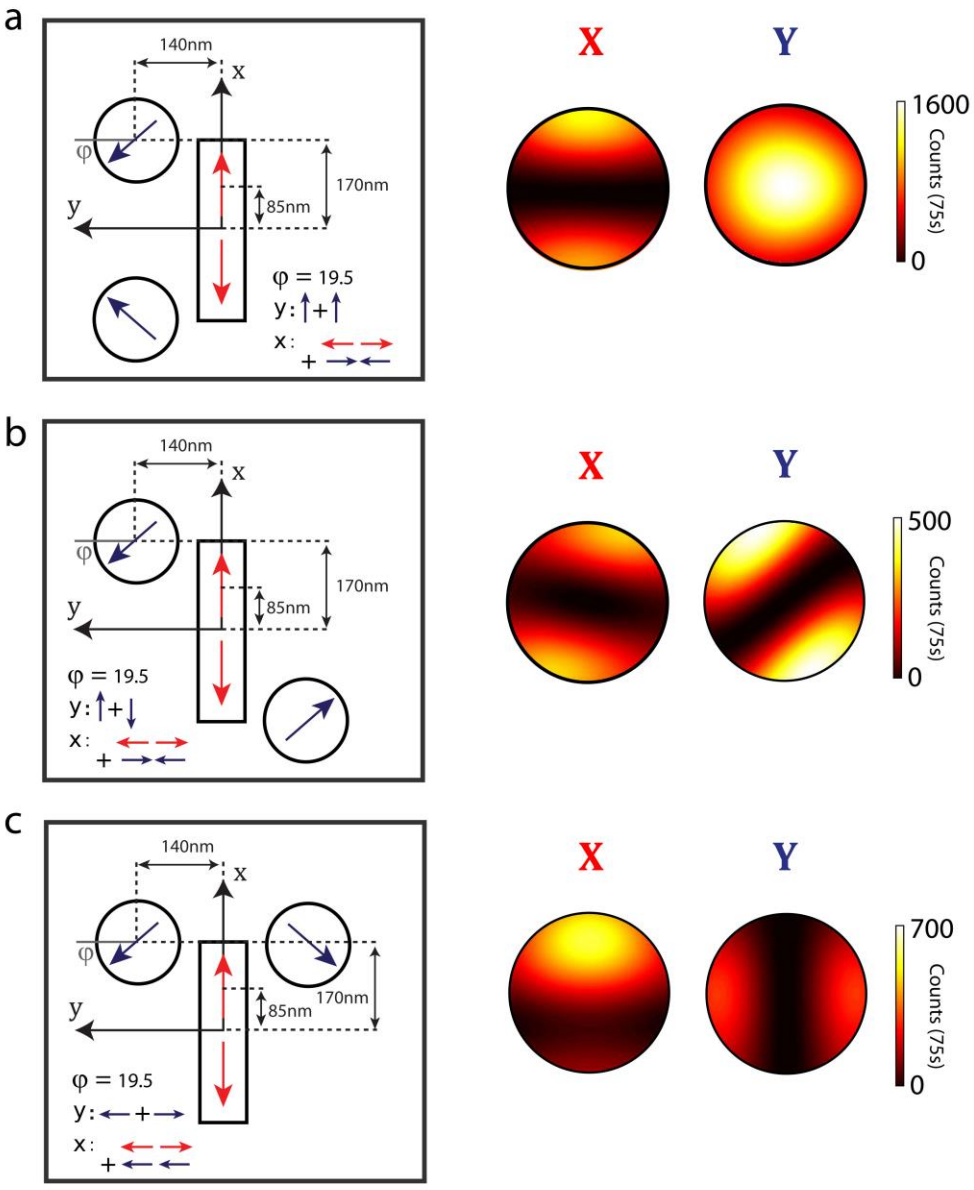

Figure 5. Dipole orientations of the antenna CIII - CV. Dipole and quadrupole orientations (left) obtained by the model required to generate the observed emission pattern and polarisation (right) for **a** CIII (cf. Fig. 4a), **b** CIV (cf. Fig. 4b) and **c** CV (cf Fig. 4c). ϕ_d is the angle between the y – axis and the disc dipole orientation. Panels on the right show the model fits to the back focal plane images in units of photon counts over 75s integration time.

It is noteworthy that the modes of CIII - CV that emit the SHG comprise of disc modes coupled to the second order mode of the bar, which produces the quadrupolar SHG of nano-antenna CI (Fig. 3a). Therefore, the characteristics of a nano-antenna's SHG can be determined by a straightforward consideration of the symmetries of the various modes at 2ω. Additional calculations and simulations of the electromagnetic fields at the nano-antenna's ω and 2ω resonances in the Supplementary Information corroborate this observation (See Figure S5 and Note 3). The optimum arrangement of 2ω-particles around the bar requires a matching of the scattering phase determined by the nonlinear surface polarisation, which is the source of SHG.

Figure 6 summarises these results by showing the contributions of the x and y polarised SHG emission from all of the nano-antennas investigated in this work. Since the quadrupolar emission is polarised along x, the y-polarised emission shows the contribution from the discs. We can confirm that the addition of a single 2ω-particle (CII) increases the proportion of bright (dipole) emission into the y polarisation. Moreover, multiple 2ω-particles increase dipolar emission further, but only in the configurations where they radiate in phase (CIII). Notably, configurations with multiple 2ω-particles can also reduce the SHG emission from the bar (CIII and CIV) due to residual out of phase dipole components along the x-direction (along the bar). Interestingly, despite being non-centro-symmetric, the CV SHG intensity is similar to a centro–symmetric structure CIV, because the dipole components interfere with the quadrupole slightly out of phase, which causes the antenna to radiate away from normal incidence.

While it could be argued that the origin of these differences, observed in Fig. 6, might also come from the tiny variation in the gaps between these nano-structures[34], relatively minor variations between repeated measurements over multiple nano-antennas of a single sample with the same lithographic exposure and from various samples were observed. This is partly because we have used 20 nm gaps between particles, which has a high reproducibility in our nanofabrication. We also note the nano-antennas CIII-CV show less antenna-antenna and sample-sample variation compared to CII, which was the most sensitive. Essentially, the variations in SHG intensity due to gap variations were minor in comparison to the variations observed due to the different configurations used.

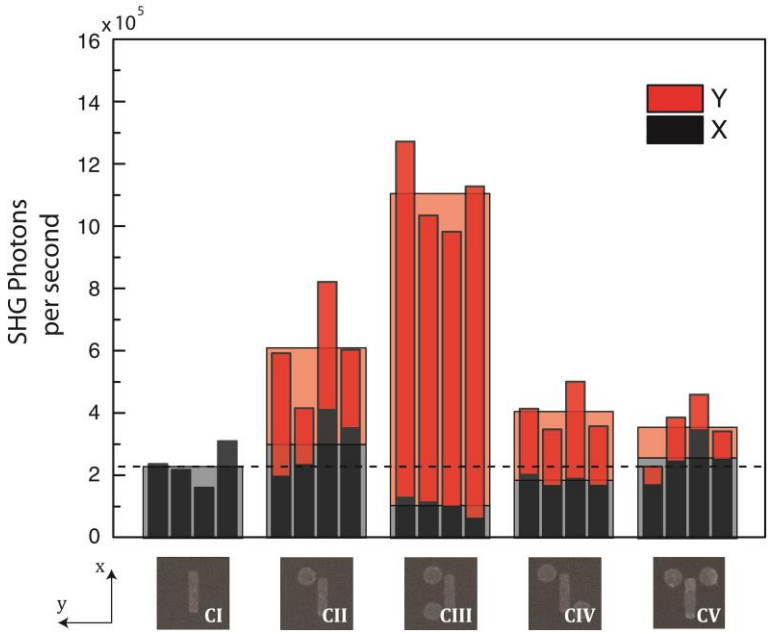

Figure 6. Contribution of x and y polarisation to the total SHG emission for the five nano-antennas considered in this work. Large (resp. small) histograms are the mean (resp. individual) values over 4 distinct nano-antennas of the same configuration.

In this article we have introduced a range of multi-resonant nano-antenna configurations that reveal the interplay of symmetry and scattering phase in SHG emission from metal nanostructures. While other works have highlighted the role of symmetry and field enhancement in antenna-driven SHG, here we identifies the relevance of dipole-quadrupole interference and scattering phase in producing highly polarised and efficient SHG. In order to maximise SHG emission in multi-resonant antennas it is important to ensure an internal phase matching of an antenna's resonant elements for directional dipolar emission with a well-defined polarisation. While this seems to be equivalent to requiring a non-centro-symmetric antenna, this is not a general rule. From a microscopic viewpoint, the interference of bright dipole and dark quadrupole sources within an antenna can drastically modify the SHG efficiency. The efficiency of SHG for a single nano-antenna in configuration CIII was found to be $\eta_{SHG} > 4 \times 10^{-7}$ W^{-1}, which corresponds to an effective $\left|\chi_{eff}^{(2)}\right| > 40$ pmV^{-1} (See Note 5). We envisage that arrays of such multi-resonant nano-antennas with strong dipole – active normal incidence SHG emission could allow highly effective exploitation of designer second order nonlinear optical processes within compact device settings.

Methods

Nano-antenna Nanofabrication

The nano-antennas were fabricated by electron beam lithography on a fused silica substrate. Firstly the substrate was coated with a positive resist (PMMA) and was baked at ~180 °C for 120 seconds. Then the nano-antennas were defined by an electron beam exposure, followed by a development procedure. Subsequently, a 1.5 nm thick Cr film was deposited by e-beam evaporation on the substrate (to increase the Au adhesion) followed by 40 nm Au film. Lift-off and Oxygen plasma were the last steps of fabrication. Linear spectroscopic characterization of the fabricated nanoparticle arrays were carried out with a Bruker Hyperion 2000 Fourier transform infrared (FTIR) microscope installed with a 36×, NA = 0.5 objective. The extinction (1 - transmission) spectra were obtained by normalizing the transmittance curve from an array-

encapsulated area with a reference spectrum taken from a bare area in close proximity to the array. Spectra were obtained in the ranges 500-1100 nm and 1100–2000 nm using a Silicon detector and Peltier cooled InGaAs detector, respectively.

Optical set-up

For the nonlinear SHG measurements, the structure was pumped by nominally >200 fs pulses at 1,500 nm, generated by the signal from a Coherent-APE Chameleon OPO, seeded by a Coherent Chameleon Ultra II. The laser was filtered by a 1000 nm cut off long pass filter (FELH1000 from Thorlabs) to suppress any lower wavelengths from the oscillator. A Dichroic mirror (DMLP1180) selectively transmits (T=95%) the 1,500 nm pump onto the sample and reflects (R=95%) the emitted SHG toward the entrance slit of a spectrometer (Acton2300) with a detection efficiency of 28%. After the sample, the pump is rejected by 1000 nm cut off short pass (FESH1000) and 750 nm bandpass filters (Fb750-10-1, T=60%). For all our measurement, our microscope objective is a Nikon S Plan Fluor ELWD 40X 0.6NA (T_{1500}=30%, T_{750} = 84%) (See Figure S1). The NA of our objective allows us to collect about 26% of any uniform forward surface scattering (approximately 2.8 times more light is scattered backward in the substrate[33]). The input polarisation of the pump is rotated via an achromatic half- wave plate 1100- 2000 nm. The output polarisation of the SHG is selected via a linear polariser (LPVIS100-MP2), which has an extinction ratio of 10^6 at 750 nm. Four extra lenses were included in the beam paths (T=72%): two lenses to correct for chromatic aberrations and two lenses to image the back focal plane. To maintain consistency, our intensity and back focal plane measurements were done within the same set-up. In all of our measurements, we used pump powers at least an order of magnitude below the damage threshold of the nano-antennas (~10 mW average power). Given the transmittance of the various components of our optical set-up, the SHG detection efficiency is estimated to be 0.4% (See Note 4).

Associated Content

Supporting Information Available: Further details on the experiment, sample characterisation, numerical simulation and calculation. This material is available free of charge via the Internet at http://pubs.acs.org.

Author Information

Notes

*These authors contributed equally to this work. The authors declare no competing financial interests.

Corresponding Author

†r.oulton@imperial.ac.uk

Acknowledgements

This work was sponsored by the EPSRC Reactive Plasmonics Programme grant (EP/M013812/1). S.A.M. further acknowledges the Royal Society and the Lee-Lucas Chair in Physics. M.N.-C. was supported by University of Birmingham (Birmingham Fellowship).

References

(1) Novotny, L.; Van Hulst, N. F. *Nat. Photonics* **2011**, *5* (2), 83–90.

(2) Shalaev, V. M. *Nat. Photonics* **2007**, *1* (1), 41–48.

(3) Soukoulis, C. M.; Wegener, M. *Nat. Photonics* **2011**, *5* (9), 1–8.

(4) Lapine, M.; Shadrivov, I. V.; Kivshar, Y. S. *Rev. Mod. Phys.* **2014**, *86* (3), 1093–1123.

(5) Zheludev, N. I.; Kivshar, Y. S. *Nat. Mater.* **2012**, *11* (11), 917–924.

(6) Li, G.; Chen, S.; Pholchai, N.; Reineke, B.; Wong, P. W. H.; Pun, E. Y. B.; Cheah, K. W.; Zentgraf, T.; Zhang, S. *Nat. Mater.* **2015**, *14* (6), 607–612.

(7) Lee, J.; Tymchenko, M.; Argyropoulos, C.; Chen, P.-Y.; Lu, F.; Demmerle, F.; Boehm, G.; Belkin, M. A.; Amann, M.; Alù, A.; Belkin, M. A. *Nature* **2014**, *511* (7507), 65–69.

(8) Segal, N.; Keren-Zur, S.; Hendler, N.; Ellenbogen, T. *Nat. Photonics* **2015**, *9* (3), 180–184.

(9) Aouani, H.; Rahmani, M.; Navarro-Cía, M.; Maier, S. A. *Nat. Nanotechnol.* **2014**, *9* (4), 290–294.

(10) Metzger, B.; Schumacher, T.; Hentschel, M.; Lippitz, M.; Giessen, H. *ACS Photonics* **2014**, *1* (6), 471–476.

(11) Celebrano, M.; Wu, X.; Baselli, M.; Großmann, S.; Biagioni, P.; Locatelli, A.; De Angelis, C.; Cerullo, G.; Osellame, R.; Hecht, B.; Duò, L.; Ciccacci, F.; Finazzi, M. *Nat. Nanotechnol.* **2015**, *10* (5), 412–417.

(12) Navarro-Cia, M.; Maier, S. a. *ACS Nano* **2012**, *6* (4), 3537–3544.

(13) Grinblat, G.; Rahmani, M.; Cortés, E.; Caldarola, M.; Comedi, D.; Maier, S. A.; Bragas, A. V. *Nano Lett.* **2014**, *14* (11), 6660–6665.

(14) Metzger, B.; Gui, L.; Fuchs, J.; Floess, D.; Hentschel, M.; Giessen, H. *Nano Lett.* **2015**, *15* (6), 3917–3922.

(15) O'Brien, K.; Suchowski, H.; Rho, J.; Salandrino, A.; Kante, B.; Yin, X.; Zhang, X. *Nat. Mater.* **2015**, *14* (4), 379–383.

(16) Utikal, T.; Zentgraf, T.; Paul, T.; Rockstuhl, C.; Lederer, F.; Lippitz, M.; Giessen, H. *Phys. Rev. Lett.* **2011**, *106* (13), 1–4.

(17) Pendry, J. B. *Science (80-.).* **2008**, *322* (5898), 71–73.

(18) Rose, A.; Smith, D. R. *Opt. Mater. Express* **2011**, *1* (7), 1232–1243.

(19) Zeuner, F.; Muldarisnur, M.; Hildebrandt, A.; Förstner, J.; Zentgraf, T. *Nano Lett.* **2015**, *15* (6), 4189–4193.

(20) Rodrigo, S. G.; Harutyunyan, H.; Novotny, L. *Phys. Rev. Lett.* **2013**, *110* (177405), 1–5.

(21) Butet, J.; Martin, O. J. F. *Opt. Express* **2014**, *22* (24), 29693–26707.

(22) Thyagarajan, K.; Butet, J.; Martin, O. J. F. *Nano Lett.* **2013**, *13* (4), 1847–1851.

(23) Gennaro, S. D.; Sonnefraud, Y.; Verellen, N.; Van Dorpe, P.; Moshchalkov, V. V.; Maier, S. A.; Oulton, R. F. *Nat. Commun.* **2014**, *5* (4748), 3748.

(24) Czaplicki, R.; Mäkitalo, J.; Siikanen, R.; Husu, H.; Lehtolahti, J.; Kuittinen, M.; Kauranen, M. *Nano Lett.* **2015**, *15* (1), 530–534.

(25) Aouani, H.; Navarro-Cia, M.; Rahmani, M.; Sidiropoulos, T. P. H.; Hong, M.; Oulton, R. F.; Maier, S. A. *Nano Lett.* **2012**, *12* (9), 4997–5002.

(26) Thyagarajan, K.; Rivier, S.; Lovera, A.; Martin, O. J. F. *Opt. Express* **2012**, *20* (12), 12860–

12865.

(27) Czaplicki, R.; Husu, H.; Siikanen, R.; Mäkitalo, J.; Kauranen, M.; Laukkanen, J.; Lehtolahti, J.; Kuittinen, M. *Phys. Rev. Lett.* **2013**, *110* (093902), 1–5.

(28) Harutyunyan, H.; Volpe, G.; Quidant, R.; Novotny, L. *Phys. Rev. Lett.* **2012**, *108* (21), 217403.

(29) Dadap, J. I.; Shan, J.; Heinz, T. F. *J. Opt. Soc. Am. B* **2004**, *21* (7), 1328–1347.

(30) Bachelier, G.; Russier-Antoine, I.; Benichou, E.; Jonin, C.; Brevet, P. *J. Opt. Soc. Am. B* **2008**, *25* (6), 955.

(31) Celebrano, M.; Savoini, M.; Biagioni, P.; Adam, P.; Duò, L.; Cerullo, G.; Finazzi, M. *Phys. Rev. B* **2009**, 2–5.

(32) Zhang, S.; Genov, D. A.; Wang, Y.; Liu, M.; Zhang, X. *Phys. Rev. Lett.* **2008**, *101* (047401), 1–4.

(33) Engheta, N.; Papas, C. H.; Elachi, C. *Radio Sci.* **1982**, *17* (6), 1557–1566.

(34) Black, L.-J.; Wiecha, P. R.; Wang, Y.; de Groot, C. H.; Paillard, V.; Girard, C.; Muskens, O. L.; Arbouet, A. *ACS Photonics* **2015**, *2* (11), 1592–1601.

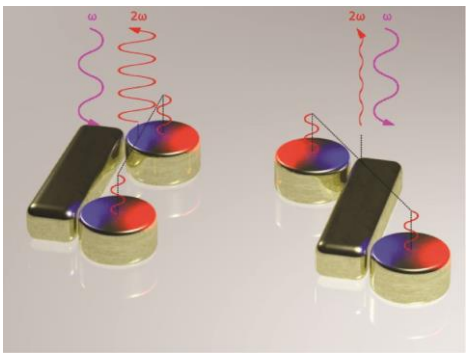

For Table of Contents only